Pulsating and Hydrodynamic Instabilities at Large Lewis Numbers

Jiao Yuan*, Yiguang Ju, and Chung K. Law
Department of Mechanical and Aerospace Engineering
Princeton University, NJ 08544, USA

Abstract

The dynamic behavior of freely propagating premixed flames with large Lewis numbers was computationally simulated using a sixth-order central difference scheme and non-reflective boundary conditions. Results in the linear stage of the instability growth show that the growth rate dramatically decreases with increasing Lewis number and that the large activation energy excites the pulsating instability and increases the growth rate of the hydrodynamic instability. In the nonlinear growth stage, there exist regimes of stable cell propagation, periodic pulsating cellular flames, and irregular pulsating cellular flames as the activation energy is increased. Characteristics of these regimes were further studied for the effects of Lewis number on the flame front structure in the stable cell propagation regime; the effects of flame pulsation on the flow and flame cell structures in the periodic pulsating cellular flame regime; and the complex pattern formation in the irregular pulsating cellular flame regime. It is further demonstrated that unsteady pulsating flames can propagate faster than the adiabatic flame when the local stretch rate is positive, implying that models based on quasi-steady flame propagation may not correctly predict the behavior of unsteady flames with large Lewis numbers.

Keywords: Lewis number, flame instability, cellular flames

* Corresponding author: yuan@princeton.edu

INTRODUCTION

There are two intrinsic instability mechanisms associated with premixed flame propagation, namely hydrodynamic instability due to the density jump across the flame front, and diffusive-thermal instability induced by the disparities between the mass and thermal diffusivities of the combustible mixture.

Hydrodynamic instability was first identified by Landau [1] and Darrieus [2], who treated the flame as an interface with a constant propagation speed, and showed that the flame is intrinsically unstable to perturbations of all wavelengths. Since stable flames do exist in the laboratory, Markstein [3] reconciled the difference by taking into account of the flame structure which has a finite thickness due to molecular diffusion. General descriptions of the effects of stretch on the flame speed and stability at near unity Lewis numbers (*Le*) were subsequently advanced by Clavin and Williams [4], Pelce and Clavin [5], and Sivashinsky [6], using large activation energy asymptotics and linear stability analysis.

Diffusive-thermal instability was first theoretically investigated by Barenblatt et al. [7], and then rigorously analyzed by Sivashinsky [8] and Joulin and Clavin [9] for adiabatic and non-adiabatic flames, respectively, based on the assumption of constant density. The dispersion relation obtained from the linear stability analysis shows that cellular instability occurs when the *Le* of the mixture is smaller than a critical value, which is slightly less than unity, while pulsating instability occurs when *Le* is larger than a critical value [8, 9] satisfying the criterion, $Ze(Le-1)>4(1+3^{1/2})\approx 10.9$ for the adiabatic flame, where $Ze = E(T_b - T_u)/T_b^2$ is the Zeldovich number. This criterion was extended by Joulin and Clavin [9] who showed that heat loss can significantly reduce the critical value. Furthermore, numerical simulation with constant density [10, 11] showed that Sivashinsky's criterion underpredicts the onset of pulsation as Le increases or Ze decreases, which is reasonable. Pulsating instability of 1D propagating flames was also studied for rich hydrogen/air [12] and lean heptane/air [13] flames, using detailed chemistry and transport. Different pulsating modes, with single and double periods, as well as pulsating extinction, were identified.

To understand the development of nonlinear flame instability, various numerical simulations based on the Navier-Stokes and the Kuromoto-Sivashinsky equations were carried out. For flames with $Le<1$, nonlinear flame instability was studied by focusing on the cellular

structure formation [6, 14, 15, 16]. Recently, more complicated phenomena on the nonlinear flame dynamics including local extinction, cell splitting, and flame lateral movement, were identified [17] for small *Le* flames. However, there have been very limited studies on the nonlinear instability development for flames with *Le*>1, which are of relevance to lean-burn situations involving hydrocarbons that contain more than two carbon atoms. In Ref. 19, two-dimensional *Le*>1 flames were simulated using the compressible Navier-Stokes equations, constant properties, and one-step reaction. Formation of the cellular flame due to hydrodynamic instability was demonstrated. However, neither pulsating instability nor traveling wave was observed. The failure to observe these instabilities was somewhat puzzling because the *Ze* used in the computation, 8.6, was well above the critical *Ze* of the Sivashinsky criterion, 10.9/(3-1)=5.45, for *Le*=3.0. On the other hand, by using a larger *Ze* of 12, Rogg [10] showed through numerical calculations the existence of pulsating instability.

Experimentally, the dynamic behavior of freely propagating premixed gaseous flame was studied recently for the large *Le*, lean butane/O_2/He mixture [20, 21]. Steadily propagating, pulsating, traveling and spinning instabilities were found to develop as the equivalence ratio of the mixture approaches the lean flammability limit. The underlying mechanisms governing such behaviors however remain unclear.

In view of the above considerations, the goal of the present study was to investigate the linear/nonlinear flame instability development at large *Le*, particularly those involving the coupling between the hydrodynamic and diffusive-thermal instabilities. In the following, we shall first simulate the linear growth of infinitesimal perturbations and determine the linear dispersion relation. The effect of pulsation on the linear growth rate of the hydrodynamic instability is investigated. Then, three different flame regimes resulting from the nonlinear coupling of the hydrodynamic and diffusive-thermal instabilities are examined.

GOVERNING EQUATIONS AND NUMERICAL SPECIFICATIONS

In this study, we simulate two-dimensional flames with one-step chemistry. The computational domain is rectangular, with the *x*- and *y*-coordinates respectively designating the directions that are perpendicular and parallel to the initial planar flame. The unburned gas is supplied from the left boundary and the flame propagates from right to left along the *x* coordinate. Unless

otherwise stated, the unperturbed flame speed and flame temperature are fixed at 3.98 m/s and 2,086 K respectively. The large flame speed was chosen because it promotes the growth rate of hydrodynamic instability so that the required computation time is significantly reduced. The activation energy normalized by the product of the universal gas constant and the unburned gas temperature (T_u = 298 K) is varied between 70 and 120, with the latter corresponding to lean combustion situations. The total length of the computational domain is 80 times of the flame thickness. The collision frequency of the chemical reaction is determined for the specified laminar flame speed as the eigenvalue of the 1D premixed propagating flame. The width of the computation domain is dictated by the number of cells and the initial cell wavelength. The above procedure in problem specification largely follows those of Kadowaki [16, 19] and Sharpe [18].

The above physical problem is modeled by the compressible N-S equations. By neglecting viscous dissipation at low Mach number in the energy equation and assuming constant transport properties, the species, momentum and energy conservation equations can be written as [22]:

$$\frac{\partial \mathbf{U}}{\partial t}+\frac{\partial \mathbf{E}}{\partial x}+\frac{\partial \mathbf{F}}{\partial y}=\frac{\partial \mathbf{E}_{\mathbf{v}}}{\partial x}+\frac{\partial \mathbf{F}_{\mathbf{v}}}{\partial y}+\mathbf{S} \tag{1}$$

where t, x and y are respectively the time and spatial coordinates, $\boldsymbol{U}$ the vector of the conservative variables, $\boldsymbol{E}$ and $\boldsymbol{F}$ the convective flux vectors in the x, y directions, $\boldsymbol{E_v}$ and $\boldsymbol{F_v}$ the corresponding diffusive flux vectors, and $\boldsymbol{S}$ the vector of the reaction source term.

$$U=\begin{bmatrix}\rho_1\\ \rho_2\\ \rho u\\ \rho v\\ E\end{bmatrix},\quad E=\begin{bmatrix}\rho_1 u\\ \rho_2 u\\ \rho uu+p\\ \rho uv\\ (E+p)u\end{bmatrix},\quad F=\begin{bmatrix}\rho_1 v\\ \rho_2 v\\ \rho uv\\ \rho vv+p\\ (E+p)v\end{bmatrix},E_V=\frac{1}{Re}\begin{bmatrix}-\rho_1 V_{1x}\\ -\rho_2 V_{2x}\\ \tau_{xx}\\ \tau_{xy}\\ q_x\end{bmatrix},\quad F_V=\frac{1}{Re}\begin{bmatrix}-\rho_1 V_{1y}\\ -\rho_2 V_{2y}\\ \tau_{yx}\\ \tau_{yy}\\ q_y\end{bmatrix},\quad S=Da\begin{bmatrix}\omega_1\\ -\omega_1\\ 0\\ 0\\ 0\end{bmatrix} \tag{2}$$

where ρ_1 and ρ_2 are, respectively, the densities of the reactant and the product, ρ the total density, u and v the velocities in x and y directions respectively, E the total energy, p the pressure, V_{ix} and V_{iy} the diffusion velocity in x and y directions, ω_1 the chemical production rate of the reactant, τ_{mn} the viscous stress, q_m the flux of heat conduction in the m direction, Re the Reynolds number and Da the Damköhler number.

The equation of state and the definition of enthalpy for the total energy are given by

$$
\begin{aligned}
p &= \rho_1 R_1 T + \rho_2 R_2 T \\
h_1 &= h_{10} + c_{p1}(T - T_0) \\
E &= \rho_1 h_1 + \rho_2 h_2 - p + \rho(u^2 + v^2)/2
\end{aligned}
\tag{3.1}
$$

Mass diffusion is modeled by the Fick's law and thermal conduction is modeled by the Fourier's law. The diffusion fluxes and the chemical reaction rate take the following forms:

$$
\begin{aligned}
&\rho_i V_{ix} = -\rho D_i \frac{\partial f_i}{\partial x} \qquad\qquad \rho_i V_{iy} = -\rho D_i \frac{\partial f_i}{\partial y} \\
&q_x = k\frac{\partial T}{\partial x} + \sum_i \rho D_i h_{0,i} \frac{\partial f_i}{\partial x} \qquad q_y = k\frac{\partial T}{\partial y} + \sum_i \rho D_i h_{0,i} \frac{\partial f_i}{\partial y} \\
&w_1 = -B\rho_1 \exp(-E_a / R^o T)
\end{aligned}
\tag{3.2}
$$

where f_i is the mass fraction of the i^{th} species, k the thermal conductivity coefficient, D_i the coefficient of binary diffusion of species i into the mixture, $h_{0,i}$ the heat of formation of species i, B the collision frequency, E_a the activation energy, and R^o the universal gas constant.

The reference quantities for nondimensionalization, designated by the subscript 0, are as follows: $l_0 = 80\delta$ is the length of the computational domain, where δ is the flame thickness. l_0 is the reference length scale; ρ_0 the density of the unburned gas and the reference density; c_0=332m/s a characteristic sound speed; $t_0 = l_0/c_0$ the reference time scale; $c_{p,0}$=1000 J/K-kg the reference specific heat; $T_0 = c_0^2/c_{p,0}$; $\mu_0 = 1.0\times10^{-4}$ J/m-s-K; $B_0 = c_0/l_0$ the reference collision frequency; $\lambda_0 = \delta$ the reference wavelength; $\Omega_0 = c_0/l_0$ the reference growth rate; $Re = l_0 c_0 \rho_0/\mu_0$ the Reynolds number, and $Da = l_0/(\rho_0 c_0)$ the Damköhler number.

Since the intrinsic flame instability is sensitive to diffusion processes, we adopt a sixth-order compact central difference scheme [25] to evaluate the convective and diffusion fluxes in Eq. 1. As such, numerical diffusion is negligible compared to physical diffusion. The governing equations were solved by this sixth-order compact central difference scheme and a third-order Runge-Kutta scheme. Pressure is calculated by the equation of state. On the upper and lower boundaries, periodic boundary conditions are applied. On the inlet boundary, flow velocity, temperature and mass fractions are specified. On the outlet boundary, non-reflective boundary conditions [26] are employed, and are briefly discussed here.

Following Refs. 23 and 27, the conservation equations 1 are first rewritten in the primitive form. By simultaneously diagonalizing the coefficient matrixes, the local one-dimensional inviscid (LODI) relations on the x boundary for non-conservative variables are obtained as,

$$\begin{aligned}
&\frac{\partial \rho_1}{\partial t} + \frac{1}{c^2}\left[W_1 + \frac{f_1}{2}(W_4 + W_5) \right] = 0 \\
&\frac{\partial \rho_2}{\partial t} + \frac{1}{c^2}\left[W_2 + \frac{f_2}{2}(W_4 + W_5) \right] = 0 \\
&\frac{\partial u}{\partial t} + \frac{1}{2\rho c}(W_4 - W_5) = 0 \\
&\frac{\partial v}{\partial t} + W_3 = 0 \\
&\frac{\partial p}{\partial t} + \frac{1}{2}(W_4 + W_5) = 0
\end{aligned} \tag{4}$$

The wave amplitude terms, $W_{1\sim5}$, are given as,

$$\begin{aligned}
W_1 &= u(c^2 \frac{\partial \rho_1}{\partial x} - f_1 \frac{\partial p}{\partial x}) \\
W_2 &= u(c^2 \frac{\partial \rho_2}{\partial x} - f_2 \frac{\partial p}{\partial x}) \\
W_3 &= u \frac{\partial v}{\partial x} \\
W_4 &= (u + c)(\frac{\partial p}{\partial x} + \rho c \frac{\partial u}{\partial x}) \\
W_5 &= (u - c)(\frac{\partial p}{\partial x} - \rho c \frac{\partial u}{\partial x})
\end{aligned} \tag{5}$$

At the right boundary for the present subsonic combustion problem, there are four outgoing waves, $W_{1\sim4}$, which are calculated by the above formulas. There is one incoming wave, W_5, which cannot be determined by the given physical boundary conditions, and is model by the formula [23],

$$W_5 = 0.25(1 - M_{\max}^2)(p - p_\infty)c / l_0 \tag{6}$$

where M_{max} is the maximum Mach number in the computational domain, p_∞ the pressure at the right infinity, c the local sound speed, and l_0 the domain size.

The above non-reflective boundary conditions for inviscid flows are different from those in [24]. Since the multi-species conservation equations and the flow equations were solved in an uncoupled manner in [24], the boundary conditions in [24] cannot recover the nonreflective

boundary conditions for the single species given by Poinsot and Lele [23]. However, in the present results, if there is only one species, the LODI relations are the same as the results of Ref. 23.

The computational domain is uniformly embedded with 801×255 grid points. In our computation, since the grid is so dense that it can successfully resolve the flame structure, the computation is stable and robust. We have carefully tested the convergence and accuracy of the current numerical method by doubling the grid density and halving the time step, and have observed that the result remained the same. Therefore, we conclude that our simulation is accurate and robust.

Computation is started by calculating the one-dimensional flame structure using the same code. The two-dimensional simulation is then conducted by adding a small initial perturbation to the one-dimensional flame structure. The influence of *Le* on flame evolution is studied by setting it to be 1.0, 1.5 and 3.0, respectively. The Prandtl number is set to be unity.

The initial perturbation is a small flame front displacement

$$\Delta = A_0 \sin(ky) \tag{7}$$

where A_0 is the perturbation magnitude and k the wave number. The global flame speed is computed as:

$$S = -\frac{1}{\rho_u Y_F L_y} \iint \omega dx dy \tag{8}$$

where ρ_u is the unburned mixture density, Y_F the fuel mass fraction of the unburned mixture, L_y the width of the computational domain, and ω the local fuel consumption rate.

RESULTS AND DISCUSSION

1. Validation of Numerical Method

In this section, we tested and verified the numerical method in three aspects: the overall spatial accuracy, the acoustic wave propagation, and the reacting flow problems.

For the overall spatial accuracy, we adopted the sixth-order compact central difference scheme for the first and second order spatial derivatives, as mentioned in the previous section. The numerical schemes for the interior points are the following:

When $3 < k < N-2$

$$\frac{1}{3}f'_{k-1} + f'_k + \frac{1}{3}f'_{k+1} = \frac{1}{h}(-\frac{1}{36}f_{k-2} - \frac{7}{9}f_{k-1} + \frac{7}{9}f_{k+1} + \frac{1}{36}f_{k+2}) \tag{9}$$

$$\frac{2}{11}f''_{k-1} + f''_k + \frac{2}{11}f''_{k+1} = \frac{1}{h^2}(\frac{3}{44}f_{k-2} + \frac{12}{11}f_{k-1} - \frac{51}{22}f_k + \frac{12}{11}f_{k+1} + \frac{3}{44}f_{k+2}) \tag{10}$$

where k is the index of the grid, N the total number of the grid in either the x or y coordinate, and h the grid size. When k=1, 2, 3 or N-2, N-1, N, the central difference scheme cannot be applied. We applied the third-order one-sided numerical differential scheme. The detailed derivation on this scheme selection can be found in Ref. 25. By applying Taylor expansion on Eq. 9, the local truncation errors are given by:

For interior grid points:

$$\left|f' - f'_{compact}\right| = C_1\Delta x^6 + ... \tag{11}$$

$$\log\left|f' - f'_{compact}\right| = 6\log\Delta x + \log C_1 \tag{12}$$

For grid points at the boundaries:

$$\left|f' - f'_{compact}\right| = C_2\Delta x^3 + ... \tag{13}$$

$$\log\left|f' - f'_{compact}\right| = 3\log\Delta x + \log C_2 \tag{14}$$

To verify the above analysis, we first numerically computed the first order derivative of the function $f = \sin x$ and compared the numerical result with the exact solution $f' = \cos x$.

In Figure 1, it is seen that when the grid size is reduced, the truncation error decreases. By measuring the gradient of the truncation error as a function of the grid size, the accuracy of the numerical method for the interior points is found to be between 4th and 5th order. For the boundary points, it is a 4th order method. Consequently, although the accuracy for the interior points is lower than that of the 6th order because of the effect of boundary conditions, the overall accuracy of the numerical method is still above 4th order.

Secondly, we tested the code by a standard shock tube problem. Here the gas in the shock tube is N_2. One half of the shock tube is filled with a high pressure N_2 at 0.2MPa, while the other half is filled with a low pressure N_2 at 0.1Mpa. The diaphragm is at the center of the shock tube and is removed at time=0. We solved this problem by using both the second-order non-MUSCL type Total Variation Diminishing (TVD) scheme and the current compact scheme, and then compare the pressure profiles at five different times (Figure 2). The pressure profiles

agreed with each other very well. This test validated that the current code can accurately compute acoustic wave propagation.

Thirdly, the numerical code was tested by two reacting flow problems: the steady and unsteady propagation of a premixed flame. For the steady premixed flame, the chemico-physical parameters for the flame are Le=3.0, Pr=1.0, E_a=70 and B=2.61×10^6. We compared the flame structure represented by the fuel mass fraction profiles from the standard PREMIX code [29] with those from the current code. In Figure 3, the profile of the fuel mass fraction of the large Le flame was compared for these two calculations because it is steeper and the computation is more challenging. It is seen that the calculated profiles overlap very well. Therefore we can conclude that the current code can compute the steady propagation of the premixed flame and predict the flame structure accurately.

For the unsteady flame propagation, we computed the 1D unsteady pulsating flame using 801 and 1601 grids, respectively. The chemical and physical parameters used are Le=3.0, Pr=1.0, E_a=120 and B= 8.285×10^9. Figure 4 shows that there is only very little difference in the calculated pulsating flame speed using the two grid sizes. Figure 5 further shows that the flame structures at time=5, 10 and 14 with different grids agree well with each other. Finally, these results remain unchanged with additional tests with further refining of the grid. These validations therefore demonstrate that the current numerical simulation is convergent and robust.

In the following simulations, we have monitored the global flame speed by Eq. 8 and adjusted the inflow boundary velocity to match the instantaneous flame speed. In this manner we were always able to keep the flame in the middle of the computational domain and minimize the effect of the boundaries.

2. Lewis Number Effect on Linear Dispersion Relation

The linear dispersion relation, representing the growth rate of an infinitesimal perturbation as a function of wave number, has been theoretically derived through large activation energy asymptotic analysis. When the activation energy is not too large as for most combustion reactions, the accuracy of the analytical results may decrease. Instead, the linear dispersion relation can be calculated through numerical simulation [18, 19]. For example, in Ref. 18 a rigorous linear dispersion relation that includes the effects of finite activation energy and arbitrary Le was obtained by using a numerical shooting method, while in Ref. 19 the linear

dispersion relation was computed by measuring the growth rate of the applied perturbation. By using the present numerical scheme which is more accurate, we have computed the dispersion relation following the approach of Ref. 19. The flame front is defined by a nondimensional temperature contour of 13.52. A small initial perturbation, set to be one tenth of the flame thickness, is superimposed on a stationary 1D flame structure. The corresponding perturbation amplitude is measured as a function of time, with it growing exponentially ($A \sim e^{\Omega t}$) with a constant growth rate Ω. In Figure 6, we chose the same parameters, Pr=0.75, Le=1.0, E_a=70 and the thermal expansion ratio ρ_u/ρ_b=6, and used the same non-dimensional references as Figure 3 of Ref. 18. We computed the dispersion relation and compared it with that of Refs. 18. It shows that the two results agree very well when the wave number is larger than the wave number corresponding to the maximum growth rate, the critical wave number. When the wave number is smaller than the critical wave number, our results are slightly smaller than those of Ref. 18. Therefore, the present result can accurately compute the dispersion relation and predict the unstable wave number range.

By varying *Le*, the effect of *Le* on the linear dispersion relation is obtained and shown in Figure 7. It is seen that when the wave number approaches zero, the growth rate also decreases to zero for all Lewis numbers. This result agrees with the theoretical prediction [6] that only the hydrodynamic effect plays an important role at small wave numbers. The results further show that, for a given *Le*, the growth rate increases when the wave number increases from zero, reaches a maximum at the critical wave number, and then decreases monotonically until it becomes negative beyond a marginal wave number. With increasing Le, the growth rate dramatically decreases while the critical and marginal wave numbers also decrease, implying the corresponding narrowing of the unstable range.

In Figure 8, the critical wave numbers determined herein are compared with those of Kadowaki [19]. The comparison is close, with the present values being slightly smaller for $Le>1$.

Our main interest here is on the effects of flame pulsating on the linear growth rate of hydrodynamic instability, which was not addressed by ref. 18 and 19. We have increased the activation energy for the Le=3.0 flame from 70 to 82 (Ze=10.04) and simulated the small initial perturbation (0.1×flame thickness) growth process for the k=0.0629 flame (Figure 9). Since Ze is above the onset of pulsating instability, the perturbation growth is expected to show the characteristics of both pulsating and hydrodynamic instabilities. Specifically, Figure 9 shows

that the flame front does not linearly move forward when it enters a pulsating cycle. Instead, the flame front is seen to move forward, stop, move backward, and then quickly move forward again. This quasi-steady cycle repeats as the bulk flame propagates forward. We shall therefore call this regime as the periodic pulsating cellular flame regime, whose characteristics will be further discussed later. The linear growth rate for the bulk flame by the dash line in Figure 9 is computed for different wave numbers and plotted in Figure 7 as open circles. The result clearly demonstrates the distinct coupling between pulsating and hydrodynamic instabilities. The growth rate with the pulsating mode coupling is larger than that of flames without the pulsating mode. Therefore, at large *Le* pulsating instability enhances the growth rate of hydrodynamic instability.

Figure 10 shows the calculated *Ze* at the onset threshold of pulsating instability of the one-dimensional planar flame. The pulsating boundary has also been numerically computed by Lasseigne et. al [11] assuming constant density. The result of Ref. [11] agrees with that of Rogg [10] when $Le>1.5$. In Figure 10, we compare our results with those of Rogg [10] and Sivashinsky's large activation energy asymptotic formula [8]. Both our and Rogg's results show that Sivashinsky's asymptotic formula underpredicts the onset threshold of pulsating instability. Furthermore, our results are consistently lower than those of Rogg [10] for *Le* varying from 1.5 to 3.0, because we considered the variable density effect. Therefore it can be concluded that the effect of variable density reduces the onset threshold of pulsating instability.

3. The Stable Cell Propagation Regime

Nonlinear effects play an important role in flame evolution. Depending on the parameter, $Ze(Le-1)$, we have found that the resulting nonlinear evolution can be categorized into three flame regimes: stable cell propagation regime, periodic pulsating cellular flame regime, and irregular pulsating cellular flame regime.

The focus of this section is to study the *Le* effect on flame evolution in the stable cell propagation regime. The *Le* varies from 1.0 to 3.0 while the wave number is kept constant at 0.0629. The amplitude of the initial perturbation is 0.8 of the flame thickness in order to promote nonlinear effects. Figure 11a shows the flame front evolution process for $Le=1.0$ from time 1 to 233. It is seen that the initial perturbation quickly grows and at time=30, the flame front has evolved from the original small sine wave to a large cellular flame structure. With

further increase in time, cell splitting occurs at the crest at time=50 due to the hydrodynamic instability. Finally, at time=233, the original perturbed two large cells split into four cells of approximately equal spacing. The wave number of the stable cell is 0.1258, which is closer to the critical wave number of the *Le*=1.0 flame, *k*=0.1853 (Figure 7) than the initial perturbation wave number (*k*=0.0629).

Similar cell splitting process also occurs for flames with larger *Le* of 1.5 and 2.0. However, with the increase of *Le*, the growth rate decreases (see Figure 7); and consequently, the splitting process is much delayed. In particular, no cell splitting occurs for *Le* larger than 3.0. For *Le*=3.0, there is no cell splitting because the initial wave number, *k*=0.0629, is closer to the critical wave number (0.0771) than 2*k*=0.1258. To confirm this observation, the initial wave number was reduced to 0.0305. In this case, cell splitting occurs for *Le*=3.0 and the final wave number is 0.0771. Therefore, it is concluded that cell splitting is favored if the wave number after the cell splitting becomes closer to the critical wave number.

After the instability development, the structures of the final stable cell for *Le*=1.0, 1.5, 2.0 and 3.0 are shown in Figure 11b. It is to be noted that for every stable cellular flame configuration, we continued our computation until the stabilization time of the final flame structure was larger than 100 and no visible change is observed. Therefore, we conclude that the structure shown in Figure 11b is stable. Since the final flame cells share the same wave number for *Le*=1.0, 1.5 and 2.0, we have compared the *Le* effect on the final flame structure. Figure 11b thus shows that, when *Le* is increased from 1.0 to 2.0, the cell depth decreases. Mechanistically, due to the converging flow at the trough, the local flame segment at the trough region has to propagate faster in order to balance the local flow speed. When *Le* is unity, the two flame elements in the trough preheat the incoming flow, yielding an increase in the local flame speed. In addition to this preheating effect, the flame also burns stronger at the trough region for *Le*>1 due to stretch effect. Therefore, the depth of the flame cell is controlled by both preheating and *Le* number effects.

4. The Periodic Pulsating Cellular Flame Regime

Since the onset of pulsating instability depends on the parameter, *Ze(Le*-1), by increasing the activation energy to a certain value for flames with *Le*>1, pulsating instability will be excited. In Section 2, Figure 9, we discussed the initial development of the hydrodynamic cells which are

also pulsating. We now investigate the subsequent situation when the hydrodynamic and pulsating instabilities are fully developed. This flame regime is designated as that of the periodic pulsating cellular flame.

Figure 12 compares the histories of the pulsating global flame speed of the two-dimensional fully developed cellular flame with that of the corresponding pulsating one-dimensional planar flame, using Le=3.0 and E_a=82. It is seen that although both flames pulsate in the periodic manner, the pulsating frequency of the 2D flame is smaller, while its mean propagation speed is larger than that of the 1D flame because its surface area is larger.

We next study the detailed evolution of the cellular structure and the flame/flow interaction in a pulsating cycle. Figure 13 illustrates the cellular flame front at time=181.1 (solid line) and 182.05 (dash line), which correspond to the lowest and highest global flame speeds in Figure 12 respectively. It is seen that at time=181.1 (Figure 14), the converging flow in the trough and the diverging flow in the crest caused by the hydrodynamics instability is established. When the flame becomes stronger and suddenly propagates forward, the thermal expansion significantly changes the flow pattern ahead of the flame, as shown by the velocity vector plot at time=182.05 in Figure 15. The flow in front of the flame crest changes its direction due to thermal expansion and this part of the flow is re-directed to the trough region. Then the flame element in the trough region is elongated to balance the incoming flow and consume more fuel. This process changes the flame cell structure and the width of the trough periodically. We also observed that the flow can even reverse its direction when the flame pulsates forward, for example at point A in front of the crest in Figure 15. Although this flow pattern is impossible for a steady situation, it is the direct result of the unsteady motion of the flame which promotes strong interaction between the flow and flame. It is an essential feature of the flow pattern in the flame pulsating cycle.

The effect of flame stretch on the local flame speed in this flame regime is also examined. According to the conventional flame stretch theory, for Le>1 flames, the flame burns stronger if the stretch rate is negative and vise versa. Figure 16a shows the computed local stretch rate [28] along the flame front defined at the constant temperature contour, 13.52, at three different times, 181.1, 181.75, and 182.05, and demonstrates that, because of the converging-diverging flow structure, the local stretch rates are negative at the trough and positive at the crest. The

corresponding local flame speeds along the flame front at these three different times have been computed by the following definition (Figure 16b),

$$S = -\frac{1}{\rho_u Y_F}\int \omega ds \tag{15}$$

where ρ_u is the unburned mixture density, Y_F the fuel mass fraction in the unburned mixture, w the local fuel consumption rate, and s the direction normal to the local flame element. Results show that at the trough the flame is the strongest and the stretch rate is negative, which is consistent with the conventional concept of stretched flames. However, at time=182.05, although the local stretch rate becomes maximum and positive at the crest, the local flame speed is larger than the planar flame speed (0.012). This result is contrary to the conventional concept of stretched flames. These results therefore suggest that, since the dependence of the local flame speed on flame stretch is sensitive to the unsteady transport process, the conventional steady-state relation between flame speed and flame stretch may not apply for strongly unsteady flames. Consequently, the extent of validity in the use of flamelet models based on quasi-steady flame description in turbulent combustion needs to be re-examined for strongly unsteady flames.

5. The Irregular Pulsating Cellular Flame Regime

When the activation energy is further increased, the local pulsation becomes so strong that it generates cellular structure and prevents stable cells from developing. We call this type of flame as the irregular pulsating cellular flame.

The flame dynamics in this regime is studied by setting the activation energy to be 120. Figure 17 compares the histories of the flame speeds between the 1D and 2D pulsating flames, showing for the 1D flame the characteristics of period doubling, which was observed and studied for rich H_2/air flames numerically [12]. For the 2D flame, however, it is seen that while the first pulsating cycle still exhibits period doubling and overlaps with the 1D flame response, the global flame speed of the 2D flame in the later pulsating cycles is distinctively different from that of the 1D flame.

To understand the effects of cellular structure on flame pulsation, the detailed 2D flame pulsation process is shown in Figure 18 by the reaction contours at time=5.7, 5.9, 6.1 and 6.3, respectively. It is seen that at time=5.7, the pulsation starts to develop. However, unlike the 1D planar flame, it does not pulsate along the entire flame front. Instead, the pulsation starts from

point (a) first, and forms one forward propagating cell at time=5.9. This cell also travels along the lateral direction shown by the arrows. Then the flame starts to pulsate at point (b) and another cell starts to develop. The two cells collide and both stop the lateral motion. The traveling waves are therefore susceptible to be annihilated by other waves propagating in the opposite direction initiated at other points. Consequently, the traveling wave due to local pulsation is irregular and cannot form a continuous pattern. Since the flame pattern depends strongly on the local condition and it changes in each pulsating cycle, the corrugated structure does not have a stable or periodic state pattern because the strong pulsating feature of the flame results in subsequent local bursts and renders the flame unstable. Furthermore, because the irregularity of the flame pattern results from local pulsations, the regular double peak pattern of the global flame speed cannot last (Figure 17). As such, we call this flame regime the regime of the irregular pulsating cellular flame**.**

6. Experimental Evidence

Experimentally, three distinct propagation regimes separated by two threshold equivalence ratios were experimentally observed for lean butane/O_2/He flames ($Le \approx 3.0$) [20, 21]. Specifically, these three regimes were respectively characterized by steady flame propagation, radial pulsation, and rotating spiral waves, which were in turn observed for fuel concentrations larger than the first threshold (1.26%), below that of the first threshold and within the range $1.21\% < X_{C4H10} < 1.25\%$, and below the second threshold value of $1.21\% < X_{C4H10} < 1.22\%$. These experiment results qualitatively agree with the three regimes identified in the present study in that regular flame cells can develop in the periodic pulsating cellular flame regime because hydrodynamic instability dominates, while corrugated flame front forms in the irregular pulsating cellular flame regime because local pulsating instability dominates. Furthermore, irregular, short time traveling wave pattern was observed in this regime because of local pulsation.

CONCLUSIONS

In this paper, the premixed flame dynamics with large *Le* was computationally studied, with emphasis on the coupling between the diffusive-thermal pulsating instability and the hydrodynamic cellular instability. We first focused on the linear instability growth stage and

computationally obtained the dispersion relation for flames with different Lewis numbers. Furthermore, we found that the flame pulsation enhances the growth rate of the hydrodynamic instability, and variable density reduces the threshold values of the *Ze* for pulsating instability. Secondly, we identified that there are three distinct flame regimes with the increase of the activation energy, namely the stable cell propagation regime, periodic pulsating cellular flame regime, and the irregular pulsating cellular flame regime. In the periodic pulsating cellular flame regime, the effects of pulsation on the flame cell structure were observed and explained by the dominant effect of hydrodynamic instability; while in the irregular pulsating cellular flame regime complicated cellular flame front formation and traveling waves along the flame front due to local pulsation were observed and explained. Regimes with similar flame dynamic were also experimentally observed for freely propagating lean butane/O_2/He flames.

Acknowledgement

This work was supported by the Air Force Office of Scientific Research and a block grant from British Petroleum Corp. and the Ford Motor Co. awarded to Princeton University on carbon mitigation and hydrogen economy.

References

1. L. Landau, *Acta Physicochim.* URSS 19 (1944) 77
2. G. Darrieus, Propagation d'un front de flamme : essai de theorie des vitesses anormales de deflagration par developpement spontane de la turbulence, communication presented at La Technique Moderne
3. G.H. Markstein, *Nonsteady Flame Propagation*, Pergamon Press (1964)
4. P. Clavin, and F.A. Williams, *J. Fluid Mech*. 116 (MAR) (1982) 251-282
5. P. Pelce, and P. Clavin, *J. Fluid Mech*. 124 (NOV) (1982) 219-237
6. G.I. Sivashinsky, *Rev. Fluid. Mech*. 15 (1983) 179-199
7. G.I. Barenblatt, Y.B. Zeldovich, and A.G. Istratov, *J. Appl. Mech. Tech. Phys.* 4 (1962) 21
8. G.I. Sivashinsky, *Combust. Sci. Technol.* 15 (3-4) (1977) 137-146
9. G. Joulin, and P. Clavin, *Combust. Flame* 35 (2) (1979) 139-153

10. B. Rogg, in *Numerical Methods in Laminar Flame Propagation*, N. Peters and J. Warnatz ed., Friedr. Vieweg & Sohn, Braunschweig/Wiesbaden, Germany, (1982) 38-48
11. D.G. Lasseignet, T.L. Jackson and L. Jameson, *Combust. Theory Modeling* 3 (1999) 591-611
12. E.C. Christiansen, C.J. Sung, and C.K., Law, *Combust. Flame* 124 (1-2) (2001) 35–49
13. E.C. Christiansen, C.K. Law, and C.J., Sung, *Proc. Combust. Inst.*28 (2000) 807–814
14. B. Denet, and P. Haldenwang, *Combust. Sci. Technol.* 86 (1-6) (1992) 199-221
15. B. Denet and J.L. Bonino, *Combust. Sci. Technol.* 99 (4-6) (1994) 235-252
16. S. Kadowaki, *Phys. Rev. E*. 56 (3) (1997) 2966-2971
17. J. Yuan, Y. Ju, C.K. Law, submitted
18. G.J. Sharpe, *Combust. Theory Modeling* 7 (2003) 45-65
19. S. Kadowaki, *Phys. Fluid.* 12 (9) (2000) 2352-2359
20. H. Pearlman, and P. Ronney, *Physics of Fluids* 6 (12) (1994) 4009-4018
21. H. Pearlman, *Combust. Flame* 109 (3) (1997) 382-398
22. Y. Ju, *AIAA Journal* 33 (8) (1995) 1418-1425
23. T. Poinsot, and S.K. Lele, *J. Compt. Phys.* 101(1) (1992) 104-129
24. M. Baum, T. Poinsot, and D. Thevenin, J. Compt. Phys.116:247-261 (1994)
25. S.K. Lele, *J. Compt. Phys.* 103(1) (1992) 16-42
26. J. Yuan, Y. Ju and C.K. Law, Proc. of the 3rd Joint Meeting of the US Sections of Combust. Inst. 27, Chicago, 2003, 1221-1228
27. K.W. Thompson, *J. Compt. Phys*, 68 (1) (1987) 1-24
28. J.B. Freund, *AIAA JOURNAL* 35 (4) (1997) 740-742
29. R.J. Kee, J.F. Grcar, M.D. Smooke, and J.A. Miller, *A Fortran Program for Modeling Steady Laminar One-Dimensional Premixed Flames*, Sandia Report SAND85-8240, 1985
30. M. Matalon, *Combust. Sci. Technol.* 31 (3-4) (1983) 169-181

Figure Captions

Figure 1 The truncation errors for the compact central scheme at the interior points and boundary points

Figure 2 The acoustic propagation in a shock tube computed by the compact central scheme and the TVD scheme. It shows the excellent agreements between the two schemes.

Figure 3 The steady laminar premixed flame structure computed by the current code and the standard PREMIX. The results overlap with each other and show the excellent agreement.

Figure 4 The comparison of the global flame speed trajectories of the 1D pulsating premixed planar flames. The 1D computational domain is embedded by 801 grids and 1601 grids, respectively.

Figure 5 The comparison of the 1D planar flame structures at time=5, 10 and 14 (marked by squares in Figure 4) using two different grids of 801 points and 1601 points. The flame structures computed by two different grids overlap with each other.

Figure 6 The comparison between the current dispersion relation and that from Ref. 18.

Figure 7 The dispersion relations of the stable cell propagation flames with Le=1.0, 1.5 and 3.0; Open circles are for Le=3.0, E_a=82 flame in the periodic pulsating cellular flame regime.

Figure 8 The critical wave numbers as a function of Le.

Figure 9 The perturbation evolution for a Le=3.0, E_a=82, k=0.629 flame in the periodic pulsating cellular flame regime at the linear growth stage.

Figure 10 The comparison of the pulsating onset boundaries.

Figure 11 (a) The cell splitting process of Le=1.0 flame.
(b) The final stable cell structures of different Le flames at Le=1.0 (solid line), 1.5 (dashed line), 2.0 (dotted line), 3.0(solid line).

Figure 12 The comparison of the global flame speed pulsation patterns between 1D and 2D flames in the periodic pulsating cellular flame regime.

Figure 13 The cell structures in a pulsating cycle for a Le=3.0 and E_a=82 flame.

Figure 14 The flow stream lines at time=181.1 for a Le=3.0 and E_a=82 flame.

Figure 15 The flow vector plot at time=182.05 for a Le=3.0 and E_a=82 flame.

Figure 16 (a) The local stretch rates at time = 181.1, 181.75 and 182.05 of the Le=3.0, E_a=82 flame.

(b) The local flame speeds at time = 181.1, 181.75 and 182.05 of the Le=3.0, E_a=82 flame.

Figure 17 The comparison of the global flame speed pulsation patterns between 1D flame and 2D flame of the Le=3.0, E_a=120 flame in the irregular pulsating cellular flame regime.

Figure 18 The local pulsation and the lateral traveling wave from time 5.7 to time 6.3 of the Le=3.0, E_a=120 flame.

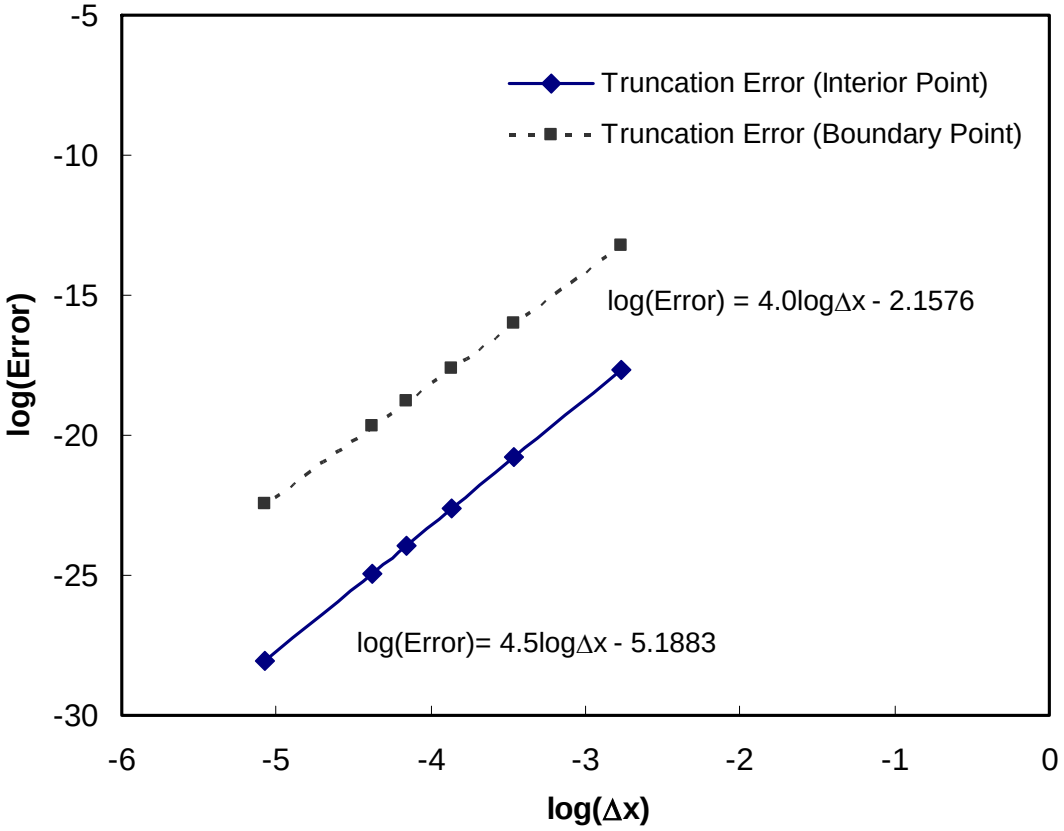
-5
-10
-15
-20
-25
-30
-6
-5
-4
-3
-2
-1
0
log(Error)
log(Δx)
Truncation Error (Interior Point)
Truncation Error (Boundary Point)
log(Error) = 4.0logΔx - 2.1576
log(Error)= 4.5logΔx - 5.1883

Figure 1

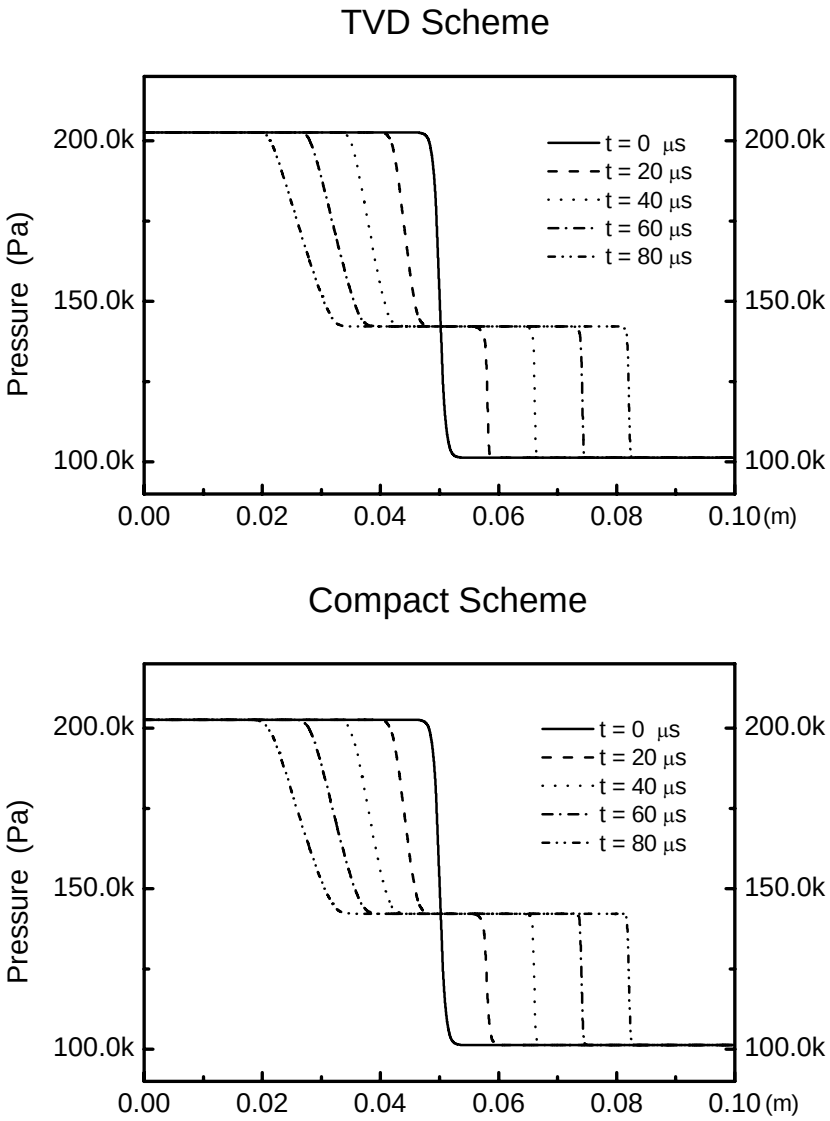

The acoustic propagation in a shock tube

Figure 2

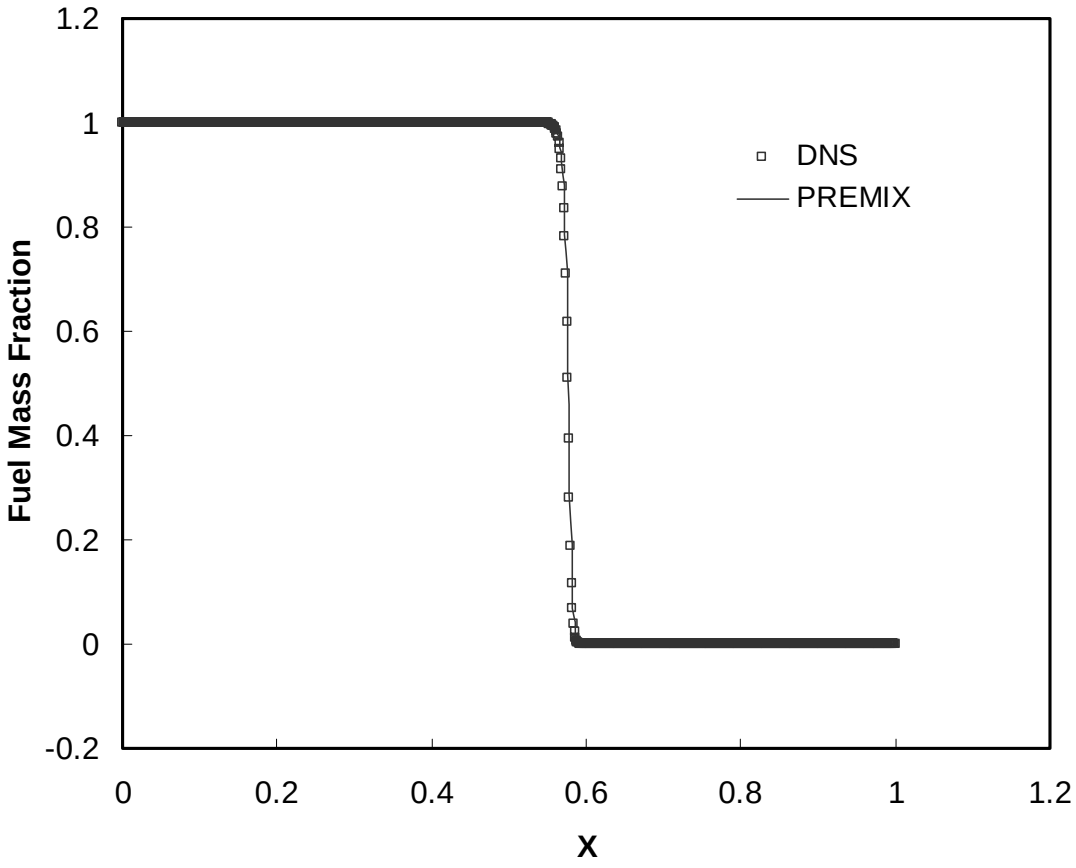
1.2
1
0.8
0.6
0.4
0.2
0
-0.2
0
0.2
0.4
0.6
0.8
1
1.2
Fuel Mass Fraction
X
DNS
PREMIX

Figure 3

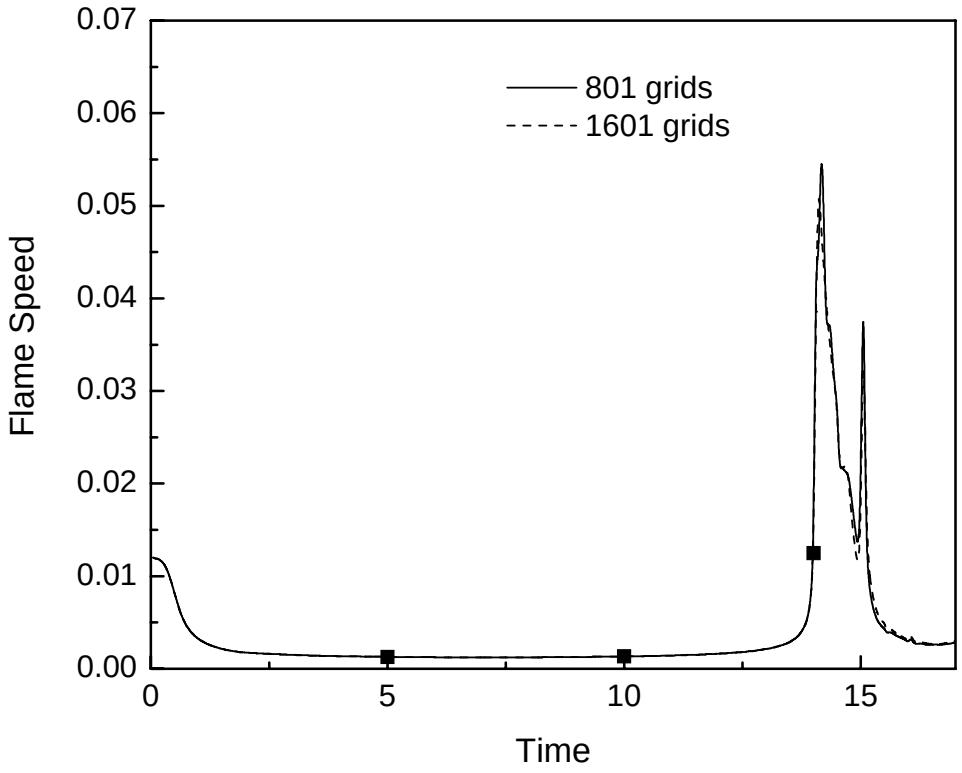
0.07
0.06
0.05
0.04
0.03
0.02
0.01
0.00
Flame Speed
801 grids
1601 grids
0
5
10
15
Time

Figure 4

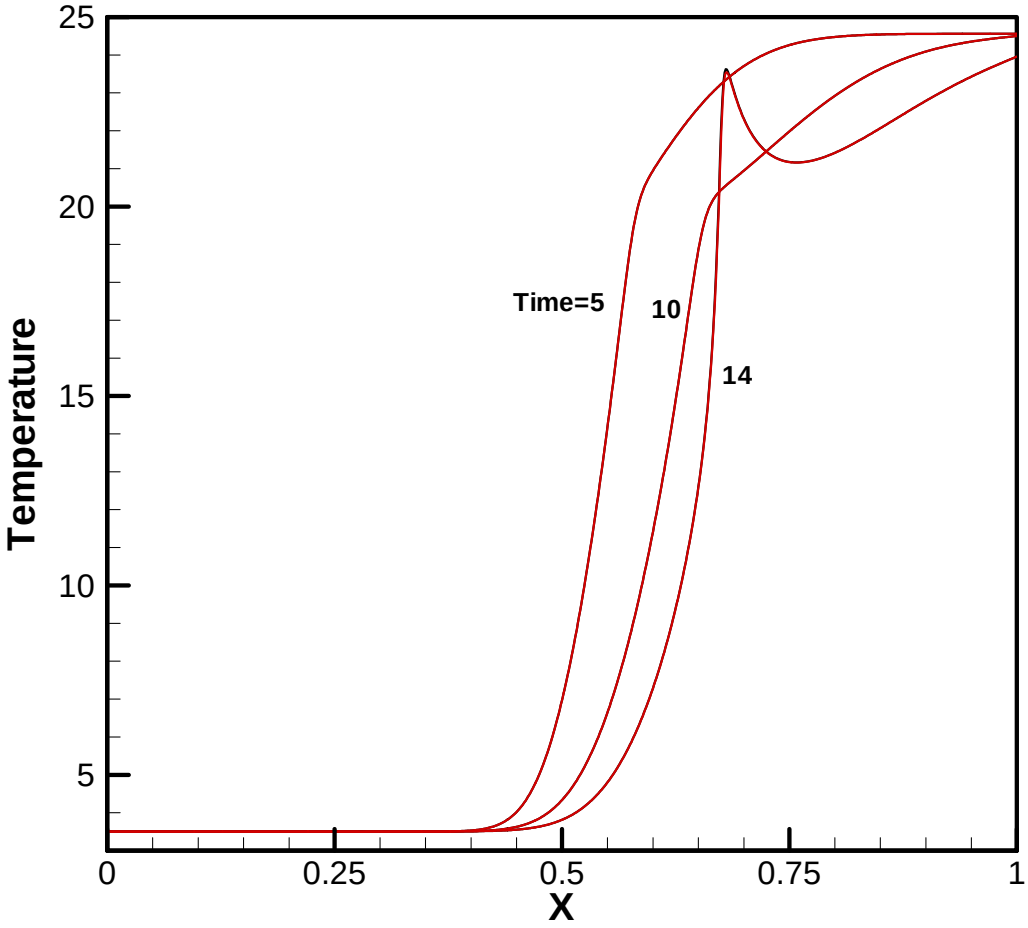

Figure 5

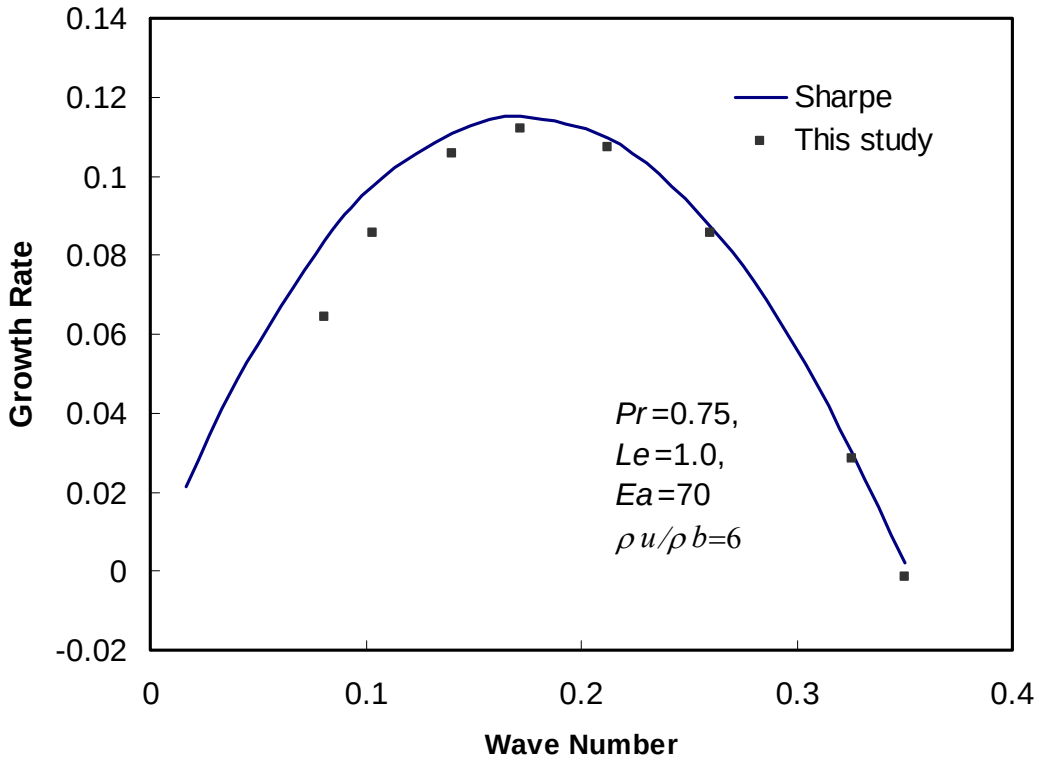
0.14
0.12
0.1
0.08
0.06
0.04
0.02
0
-0.02
Growth Rate
0
0.1
0.2
0.3
0.4
Wave Number
Sharpe
This study
Pr=0.75,
Le=1.0,
Ea=70
ρu/ρb=6

Figure 6

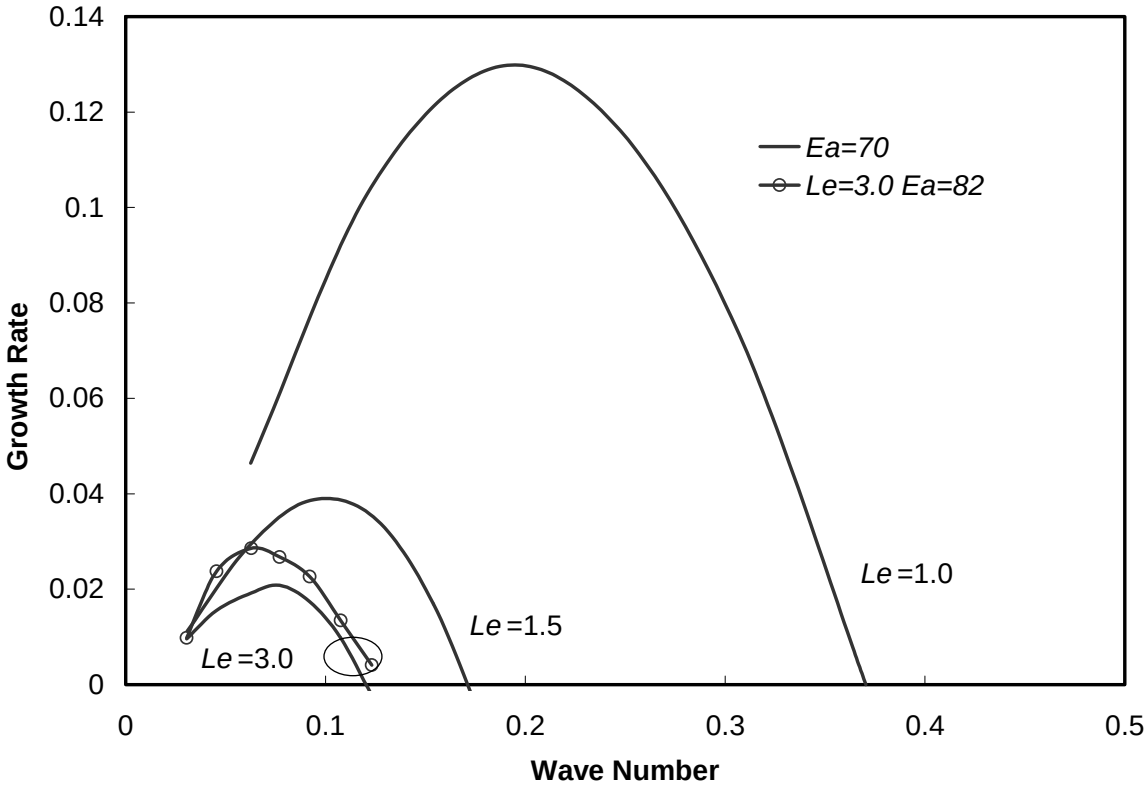
0.14
0.12
0.1
0.08
0.06
0.04
0.02
0
Growth Rate
0
0.1
0.2
0.3
0.4
0.5
Wave Number
Ea=70
Le=3.0 Ea=82
Le =1.0
Le =1.5
Le =3.0

Figure 7

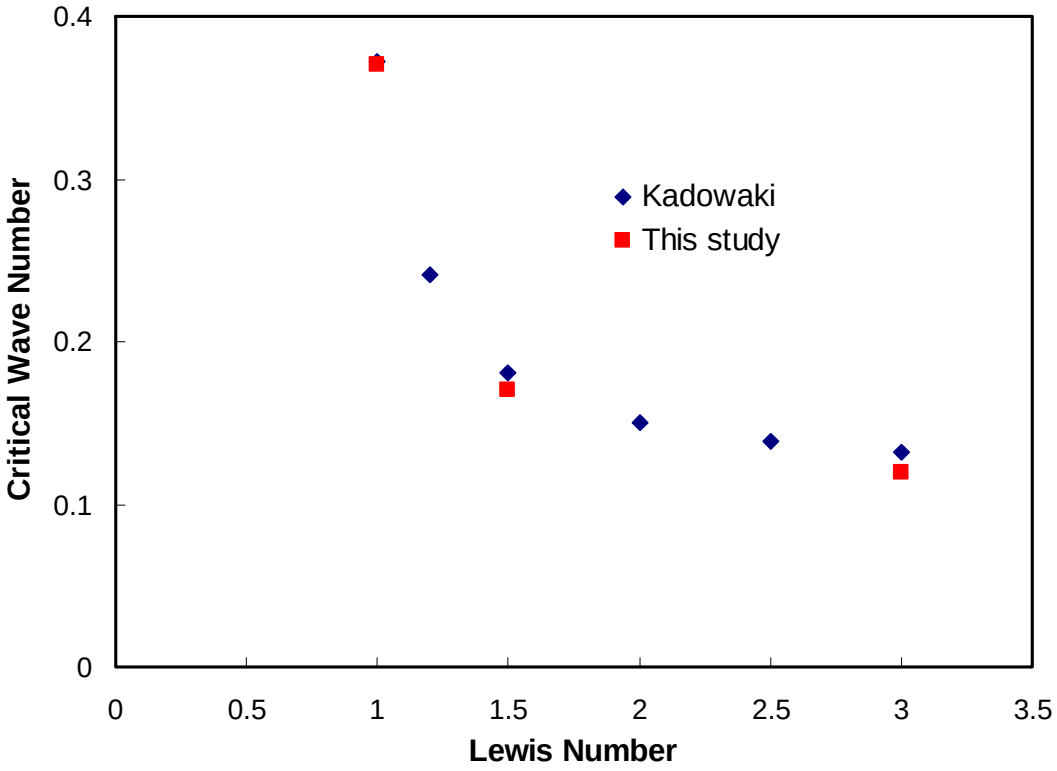
0.4
0.3
0.2
0.1
0
Critical Wave Number
0
0.5
1
1.5
2
2.5
3
3.5
Lewis Number
Kadowaki
This study

Figure 8

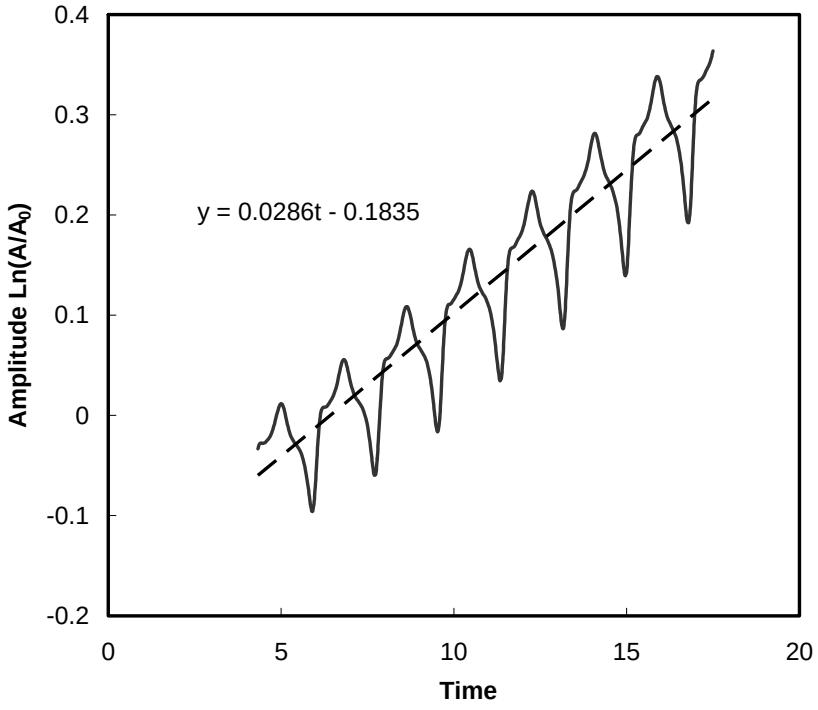
0.4
0.3
0.2
0.1
0
-0.1
-0.2
0
5
10
15
20
Amplitude Ln(A/A0)
Time
y = 0.0286t - 0.1835

Figure 9

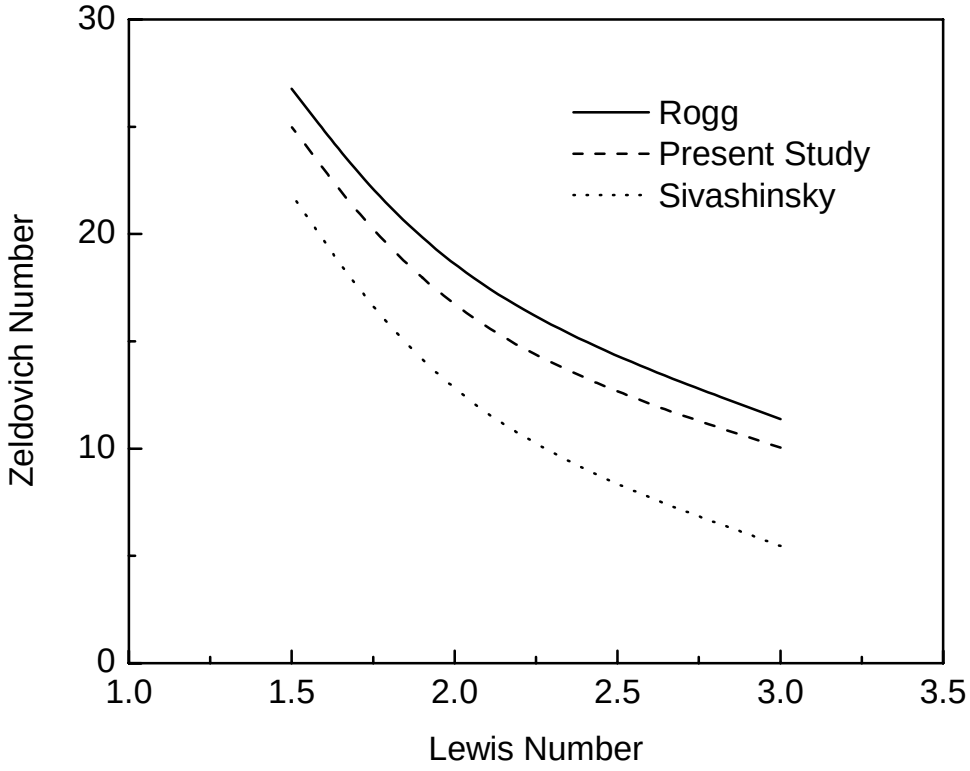
30
20
10
0
1.0
1.5
2.0
2.5
3.0
3.5
Zeldovich Number
Lewis Number
Rogg
Present Study
Sivashinsky

Figure 10

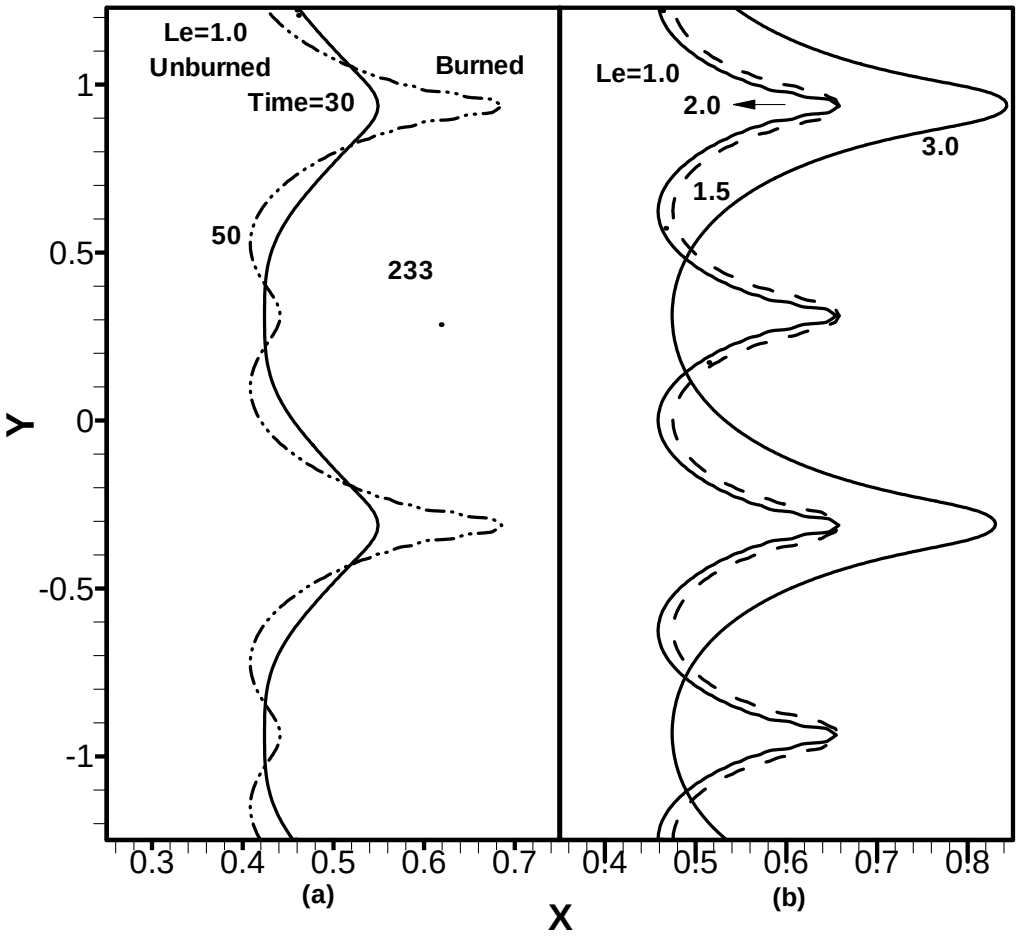
Le=1.0
Unburned
Burned
Time=30
50
233
Le=1.0
2.0
3.0
1.5
Y
X
(a)
(b)
1
0.5
0
-0.5
-1
0.3
0.4
0.5
0.6
0.7
0.4
0.5
0.6
0.7
0.8

Figure 11

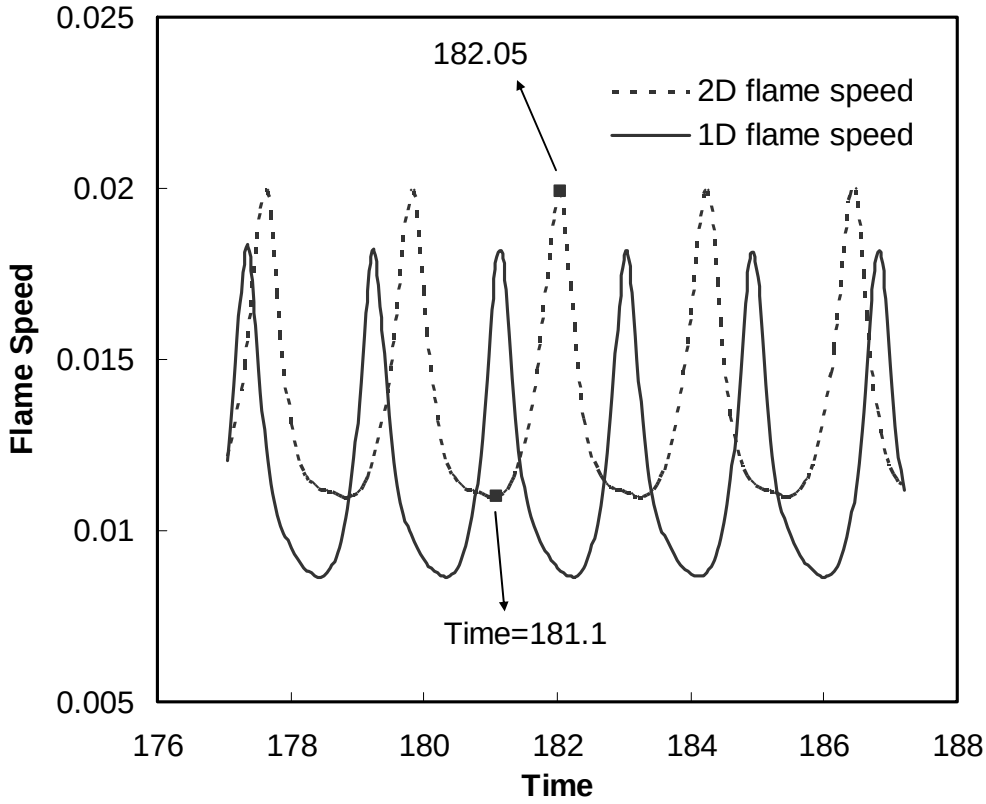
0.025
0.02
0.015
0.01
0.005
Flame Speed
182.05
2D flame speed
1D flame speed
Time=181.1
176
178
180
182
184
186
188
Time

Figure 12

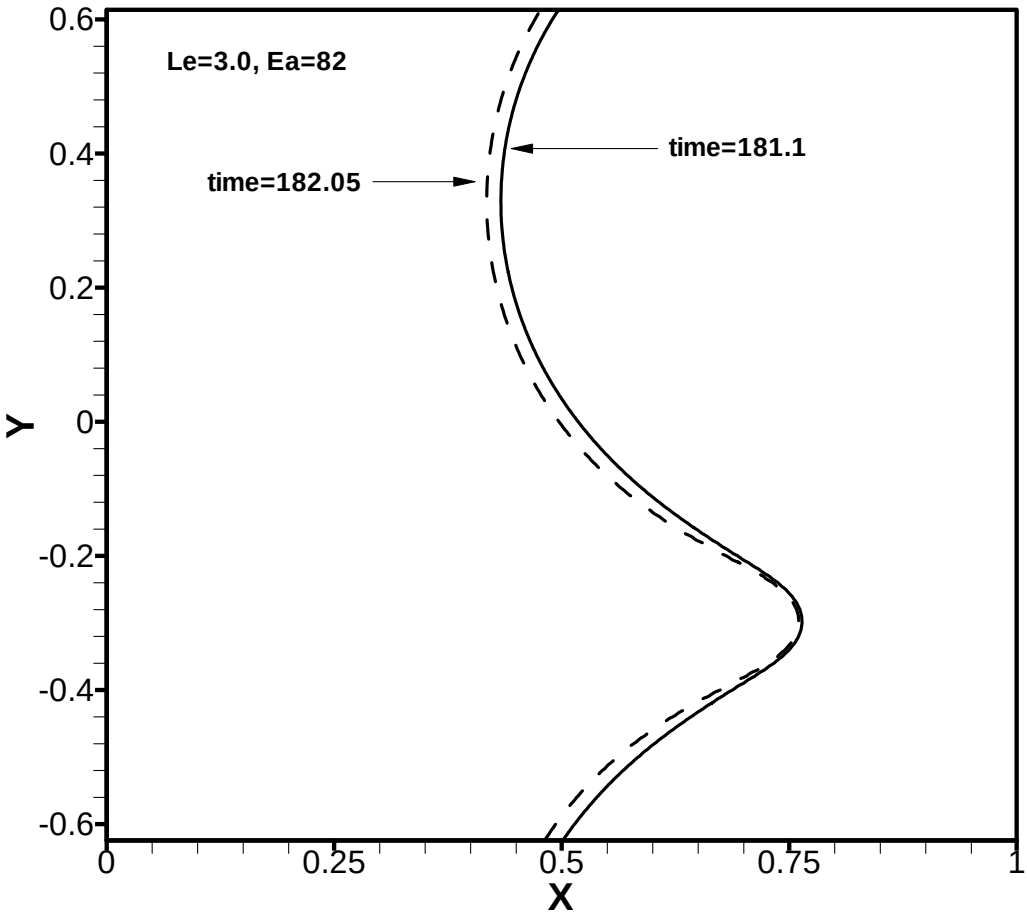
Le=3.0, Ea=82
time=181.1
time=182.05
0.6
0.4
0.2
0
-0.2
-0.4
-0.6
Y
0
0.25
0.5
0.75
1
X

Figure 13

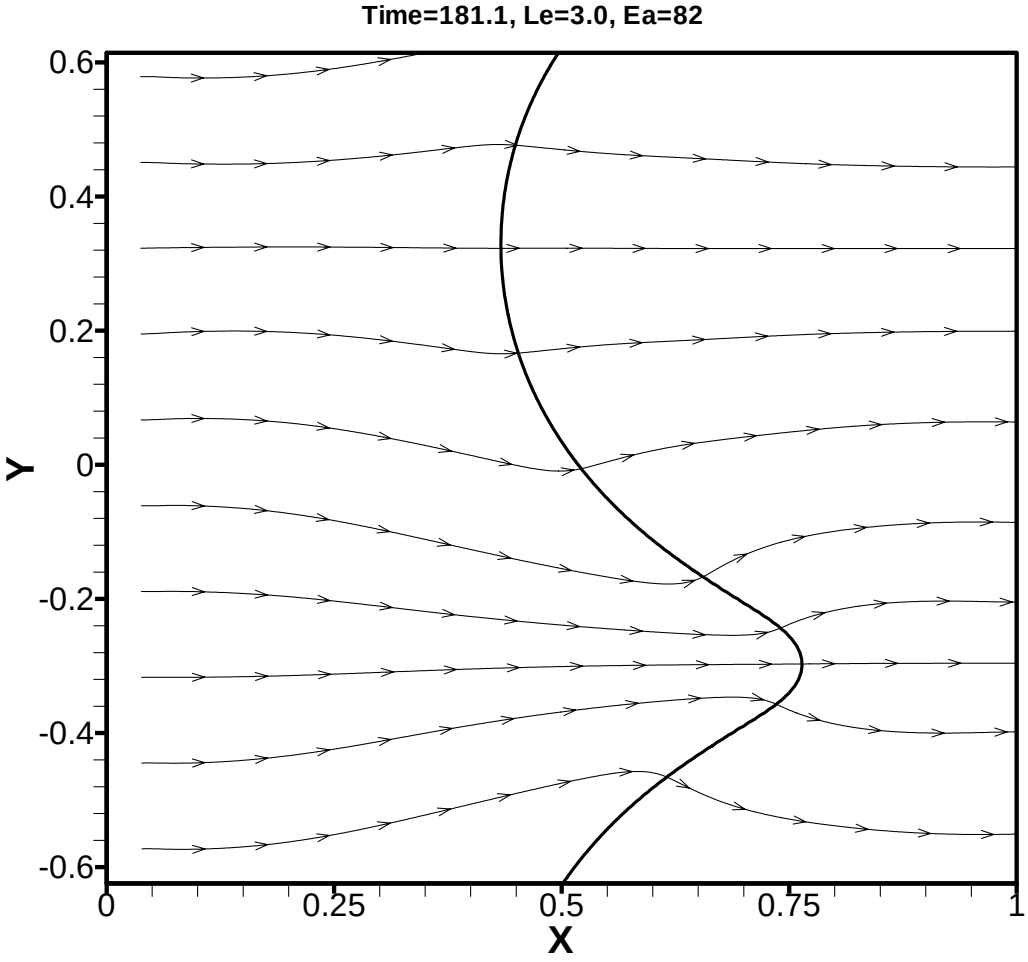

Figure 14

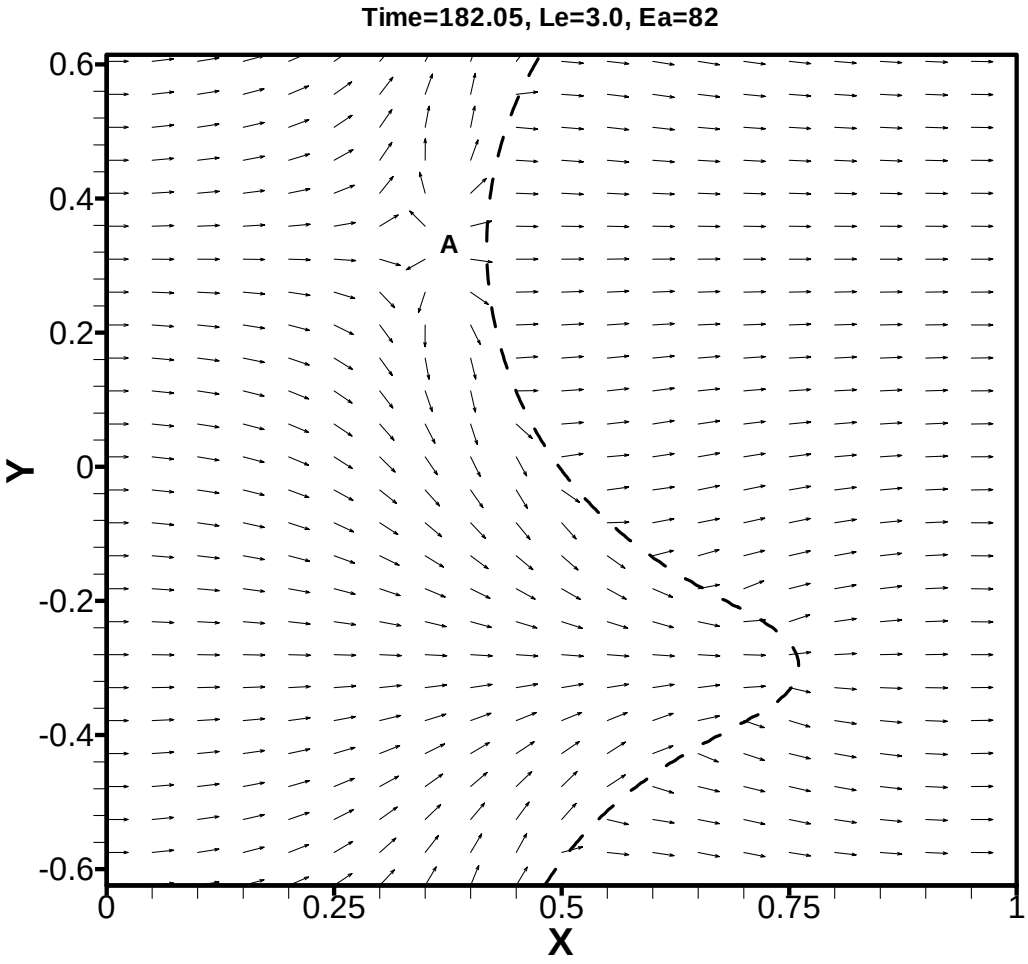

Figure 15

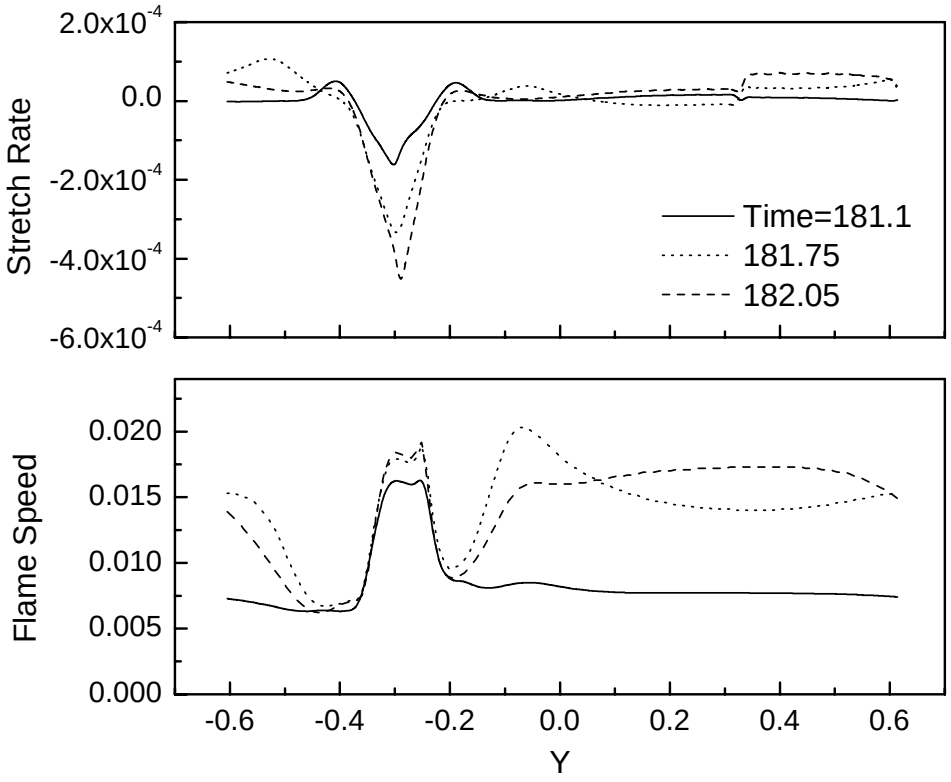
2.0x10-4
0.0
-2.0x10-4
-4.0x10-4
-6.0x10-4
Stretch Rate
Time=181.1
181.75
182.05
0.020
0.015
0.010
0.005
0.000
Flame Speed
-0.6
-0.4
-0.2
0.0
0.2
0.4
0.6
Y

Figure 16

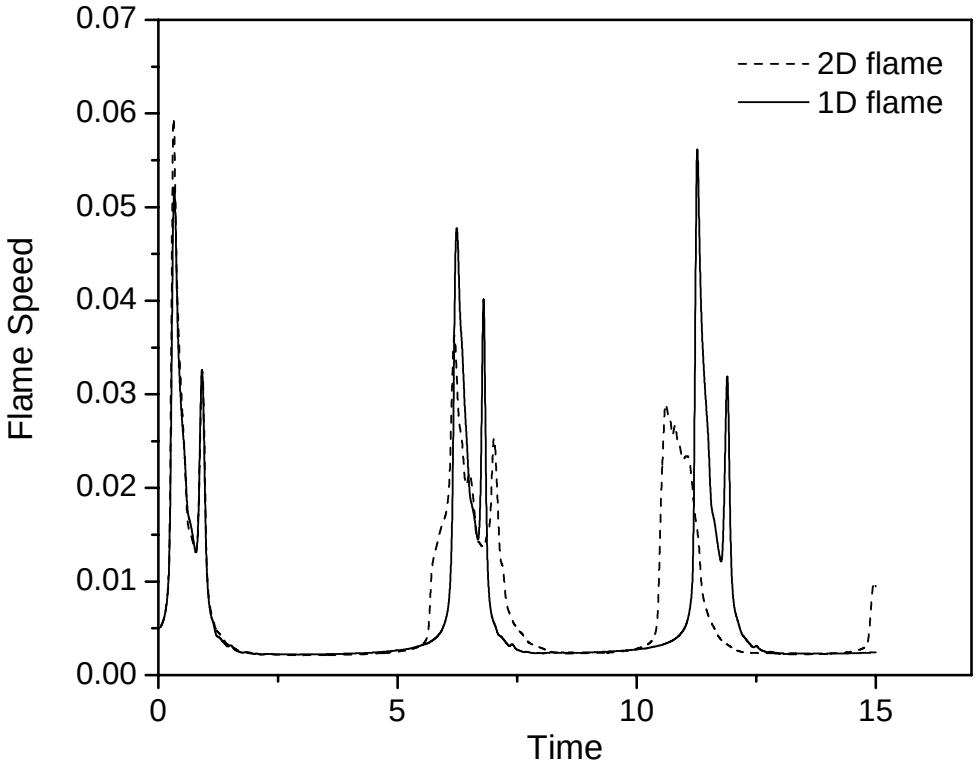
0.07
0.06
0.05
0.04
0.03
0.02
0.01
0.00
Flame Speed
0
5
10
15
Time
2D flame
1D flame

Figure 17

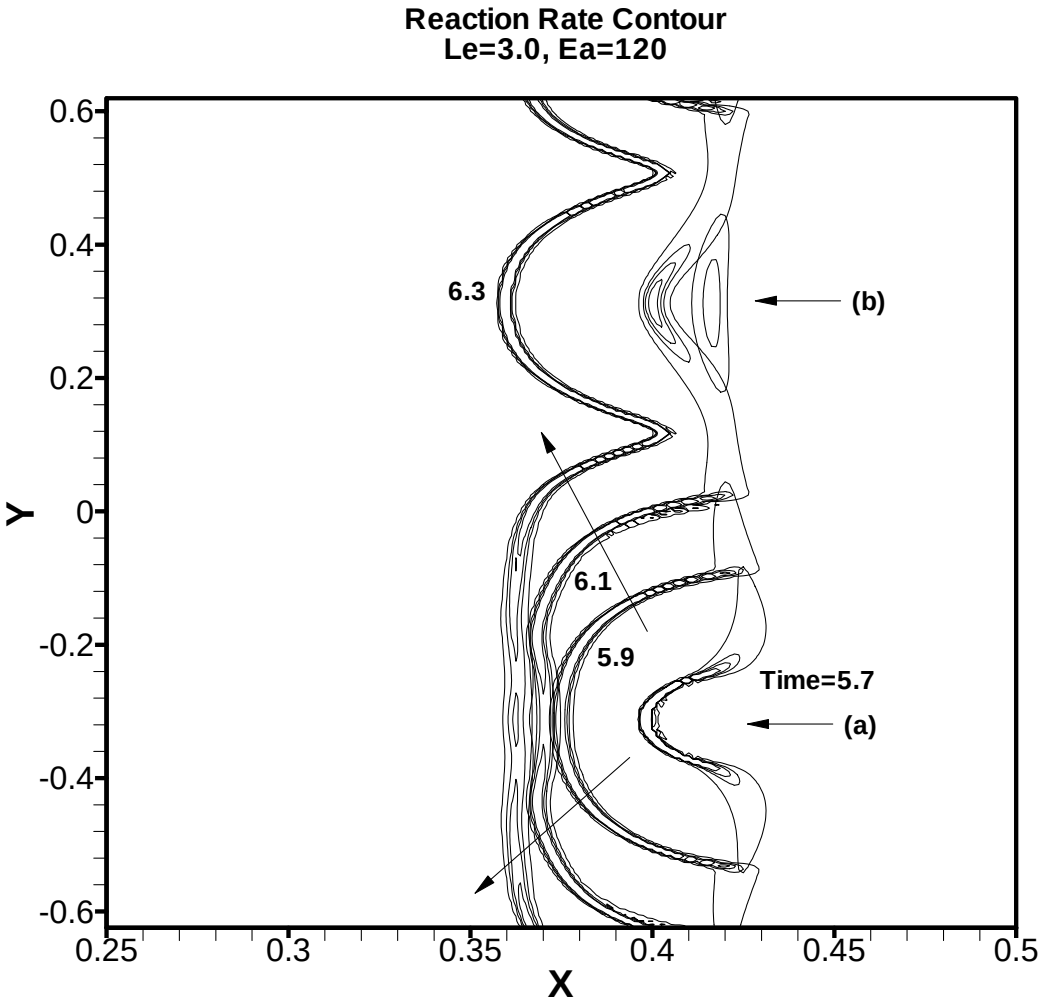
Reaction Rate Contour
Le=3.0, Ea=120
6.3
(b)
6.1
5.9
Time=5.7
(a)
Y
X
0.6
0.4
0.2
0
-0.2
-0.4
-0.6
0.25
0.3
0.35
0.4
0.45
0.5

Figure 18